Journal of Applied Electrochemistry (2005) 35:217–227
DOI 10.1007/s10800-004-6304-7

Electrochemical and AFM study of Zn electrodeposition in the presence of benzylideneacetone in a chloride-based acidic bath

P. DÍAZ-ARISTA, Y. MEAS, R. ORTEGA and G. TREJO*
Centro de Investigación y Desarrollo Tecnológico en Electroquímica (CIDETEQ), Parque Tecnológico Sanfandila, Pedro Escobedo, Querétaro, A.P. 064. C.P. 76700, Querétaro, México
*(*author for correspondence, e-mail: gtrejo@cideteq.mx)*

Received 05 January 2004; accepted in revised form 11 November 2004

Key words: additives, benzylideneacetone, electrodeposition, electrocrystallization, zinc

Abstract

The influence of benzylideneacetone (BDA) on the mechanism of zinc deposition and nucleation was studied by voltammetry, chronoamperometry and atomic force microscopy (AFM). The addition of BDA to the electrolyte solution partially inhibited (97%) the reduction of zinc at the potential $E = -1.15$ vs SCE/V, giving rise to an increase in the overpotential for the discharge of the metal ion. This leads to the existence of two reduction processes with different energies that involve the same species, $ZnCl_4^{2-}$. Analysis of chronoamperograms obtained in the absence and presence of BDA indicates that distinct nucleation mechanisms are involved during the initial stages of Zn deposition. In the absence of BDA, the transients are consistent with the model of 3D diffusion-controlled nucleation. In the presence of BDA, the transients exhibit a more complex form involving two growth processes. The first process, which occurs at short times, is explained in terms of a combination of three simultaneous nucleation processes: 2D progressive, 2D instantaneous, and 3D progressive nucleation, each limited by the incorporation of adatoms. The second process, which occurs at longer times, involves the three processes that occur at short times in conjunction with a principal contribution from a diffusion-controlled 3D nucleation mechanism. AFM imaging shows that the morphology of the deposited zinc depends on the applied electrode potential.

1. Introduction

Zinc electrodeposits are of practical and industrial importance due to their proven ability to protect ferrous substrates against corrosion [1–5]. Diverse factors influence the mechanism of zinc electrodeposition, including the morphology of the coating that is formed. Recent work by Raeissi et al. [6] showed that temperature, pH, and current density affect the morphology and texture, as well as the nucleation mechanism, of zinc deposits. Yu et al. [7] observed that increasing the temperature increased the nucleation density and modified the nucleation mechanism of zinc electrodeposits. In addition, it has been shown that the concentration of zinc ions [8], complexing agents [9], anions [10, 11] and organic additives [12] play fundamental roles in zinc electrodeposition. The use of additives in electrolytic baths is very important due to their influence on the growth and structure of the deposits obtained. Typically, additives are added to the electrolytic bath at concentrations on the order of parts per million; their presence in the bath promotes the formation of soft and shiny coatings. In recent years benzoic acid (BA) and benzylideneacetone (BDA) have been increasingly used as additives in the electrodeposition of zinc [13, 14] and zinc–cobalt alloys [15] in acid baths. The superior quality of the coatings obtained in the presence of these additives has generated growing interest in the effects of these compounds on the morphology and physical properties of the coatings. Recent studies by Su-Moon and co-workers [16, 17] have shown that BA controls the roughness of zinc coatings, an effect that was attributed to the adsorption of BA onto active sites on the substrate. Danciu et al. [18] reported similar results when BDA was used as a primary brightener in the electrodeposition of zinc coatings. They showed that addition of a range of brighteners, including BDA, caused a significant displacement of the potentiodynamic curves toward more negative potentials. In other work in this area, Juhos et al. [19] showed that addition of BDA increases the capacitance of the double layer, and Bernotiene et al. [14, 20], in a study of the behavior of BDA during zinc electrodeposition, found that addition of BA into the bath caused a decrease in the rate of BDA consumption.

The aim of the present work was to study the influence of BDA on the mechanism of zinc reduction and nucleation in chloride-based acidic media. This was achieved through an electrochemical study using cyclic voltammetry (CV) and chronoamperometry, in

conjunction with imaging of the surface morphology by atomic force microscopy (AFM) in air (*ex situ*).

2. Experimental details

CV and chronoamperometry, as well as AFM in contact mode, were used to study the mechanism of zinc electrodeposition onto Pt. The electrochemical study was carried out in a conventional three-electrode cell. The working electrode was a platinum disc of surface area 0.035 cm^2 enclosed in Teflon, and the Pt surface was polished to a mirror finish with 0.05 μm alumina powder (Buehler). A saturated calomel electrode (SCE) was used as the reference electrode, and a Pt rod was used as the counter electrode. All potentials reported here are expressed with respect to the SCE. The electrochemical experiments were controlled using a Potentiostat/Galvanostat PAR (Mod. 273A) coupled to a computer running the data acquisition software M-270 (PAR). The electrodeposition of zinc was carried out in a base solution (S_0) of composition: 0.1 M $ZnCl_2$ + 0.32 M H_3BO_4 + 2.8 M KCl, pH = 5.0. The influence of BDA was studied at two concentrations of this additive, 0.2 and 0.3 g l^{-1}. All solutions were prepared using analytical grade reagents purchased from Aldrich. Before each electrochemical experiment, the solution was deoxygenated for 30 min with ultrapure nitrogen. AFM (Digital Instruments, Mod. Nanoscope E) in contact mode was used to obtain images of the zinc deposits on Pt. Measurements were performed in air (*ex situ*) using a platinum plate (Arrandee) as the working electrode and silicon nitride AFM tips (Digital Instruments). All images were obtained at 1 Hz and are represented in the so-called height mode, in which the highest part appears brighter.

3. Results and discussion

3.1. *Voltammetric study*

To determine the effect of BDA on the process of zinc reduction, voltammetric studies in the potential range of 0.0 to −1.35 vs SCE/V in solutions S_0 (0.1 M $ZnCl_2$ + 0.32 M H_3BO_4 + 2.8 M KCl, pH = 5.0) and S_0 + BDA were carried out. The potential scan was initiated in the cathodic direction from the rest potential (E_{rest}) with a potential scan rate (v) of 30 mV s^{-1}.

3.1.1. *Voltammetric study without BDA*

Figure 1 shows a typical voltammogram obtained from solution S_0. During the potential scan in the cathodic direction, a reduction peak, Ic, whose peak potential (E_{PIc}) has a value of −1.15 vs SCE/V, is formed; this peak is associated with the reduction of Zn(II) to Zn(0). Previous studies [8] have demonstrated that the reduction process associated with this peak is controlled by mass transfer.

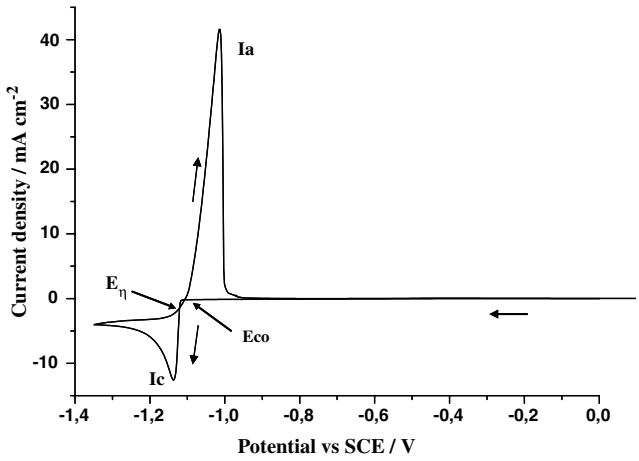

Fig. 1. Typical voltammogram obtained in solution S_0 (composition: 0.1 M $ZnCl_2$ + 0.32 M H_3BO_3 + 2.8 M KCl, pH = 5.0) at v = 30 mV s^{-1}.

On switching the potential scan at −1.35 vs SCE/V and scanning in the anodic direction, two crossovers are observed between the current densities of the scans in the cathodic and anodic directions. The potential at which the more cathodic crossover occurs is known as the nucleation overpotential (E_η) [21]. The second crossover, which occurs at −1.094 vs SCE/V, is known as the crossover potential (Eco) [22]. The appearance of these two crossovers is characteristic of processes involving nucleation [23]. At potentials more anodic than Eco, an anodic peak (Ia) appears, which is associated with the oxidation of Zn(0) formed during the cathodic scan.

The behavior of Eco was studied using the switching potential technique [24, 25]. In this technique, the switching potential (E_λ) is fixed at the foot of the reduction peak Ic and the potential scan is switched to the anodic direction. Figure 2 shows the voltammograms obtained under these conditions. When E_λ is

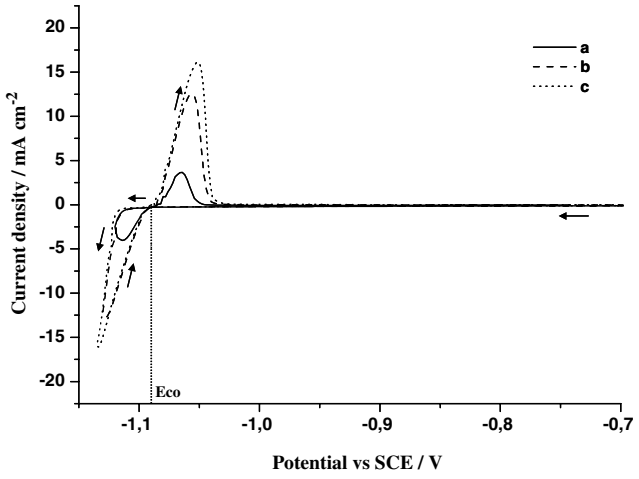

Fig. 2. Typical voltammograms for zinc nucleation on Pt, showing the crossover potential (Eco), obtained in solution S_0 at different switching potentials (E_λ). (a) E_λ = −1.12, (b) E_λ = −1.13, (c) E_λ = −1.14 vs SCE/V.

successively switched in the potential range −1.12 to −1.14 vs SCE/V, the value of Eco remains constant (= −1.092 vs SCE/V). Fletcher et al. [21, 22] proposed that when Eco is independent of E_λ, Eco corresponds to the conditional potential for the metal ion/metal system involved ($\mathrm{Eco} = E'_{M^{n+}/M}$). The value of Eco obtained using this approximation is very close to the value of the conditional potential (E') calculated using the following Nernst-type equation reported [8] for the system $ZnCl_4^{2-}/Zn(0)$:

$$E'_{ZnCl_4^{2-}/Zn(0)} = -1.01 + 0.12\mathrm{pCl} - 0.03\mathrm{pZn}' \qquad (1)$$

For the working conditions used in the present study ($\mathrm{pCl}' = -0.45$, $\mathrm{pZn}' = 1.0$, pH = 5.0), $E'_{ZnCl_4^{2-}/Zn(0)} = -1.094$ vs SCE/V. Thus, under these conditions the zinc reduction process occurs via the following reaction:

$$ZnCl_4^{2-} + 2e^- \rightarrow Zn(0) + 4Cl^- \qquad (2)$$

3.1.2. *Voltammetric study in the presence of BDA*

Figure 3 shows the voltammograms obtained at the two BDA concentrations used in this study (0.2 and 0.3 g l^{-1} BDA). The presence of BDA in the base solution S_0 causes significant changes in the behavior of the voltammograms. Two reduction peaks are clearly observed: a small peak, I'c, at −1.15 vs SCE/V, and a much larger peak (peak II'c) at more negative potentials. The potential at which peak I'c (EPI'c = −1.15 vs SCE/V) appears is the same as that obtained during the reduction of zinc in the absence of BDA (Peak Ic, Figure 1). Thus, the formation of peak I'c when BDA is present in the solution is associated with the inhibition of zinc reduction at this potential. Increasing the BDA concentration from 0.2 to 0.3 g l^{-1} has no effect on the current density ($i_{PI'c}$) or the potential of peak I'c ($E_{PI'c}$). At potentials more cathodic than $E_{PI'c}$, the cathodic current density approaches zero and remains constant over a potential range that depends on the concentration of BDA. Subsequently, the formation of the second reduction peak (associated with the bulk deposition of Zn) is observed (peak II'c), whose peak potential ($E_{PII'c}$) is displaced to a more negative potential on increasing the BDA concentration. This cathodic displacement effect, known as cathodic polarization, has been reported for other organic compounds [26, 27].

The behavior observed during the reduction of Zn in the presence of BDA is associated with the adsorption of the additive onto the Pt surface. The adsorbed BDA forms an adlayer that almost completely inhibits the discharge of the Zn(II) ion, and blocks most of the active sites at which the first reduction process (peak I'c) occurs. Subsequently, an increase in the overpotential is required for the desorption of BDA from the Pt surface, allowing the reduction of Zn(II) to take place (Peak II'c) at the active sites vacated by the BDA molecules. Mockute et al. [20] have shown that during the electrolysis of Zn in baths containing BDA, the additive is adsorbed onto the electrode surface and decomposes into diverse compounds. These reaction products and the unreacted BDA partially block the active sites on Pt at which Zn deposition occurs.

When the potential scan is switched to the anodic direction at −1.35 vs SCE/V, two crossovers, characteristic of processes that involve the formation of a new phase, are observed. Additionally, in the potential interval used in these experiments, only one oxidation peak (I'a) is observed during the anodic scan.

Further experiments in which the potential scan was switched to the anodic direction at different values of E_λ, fixed at the foot of reduction peak I'c or II'c (e.g. $E_\lambda > E_{PI'c}$, $E_\lambda > E_{PII'c}$), revealed that the current density of peak I'a depends on both reduction peaks (Figure 4). When the potential scan was switched to the anodic direction at the potential at the foot of peak II'c ($E_\lambda > E_{PII'c}$), the form of peak I'a became complex, probably due to the dissolution of the different zinc

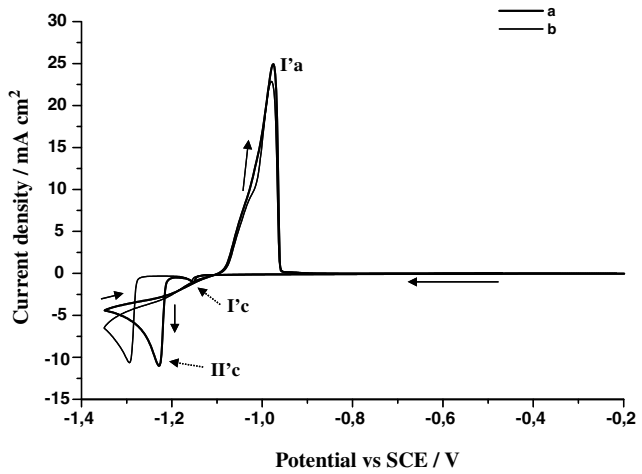

Fig. 3. Typical voltammogram obtained on Pt in solution S_0 with two concentrations of BDA. (a) 0.2 g l^{-1}, (b) 0.3 g l^{-1} at $v = 30$ mV s^{-1}.

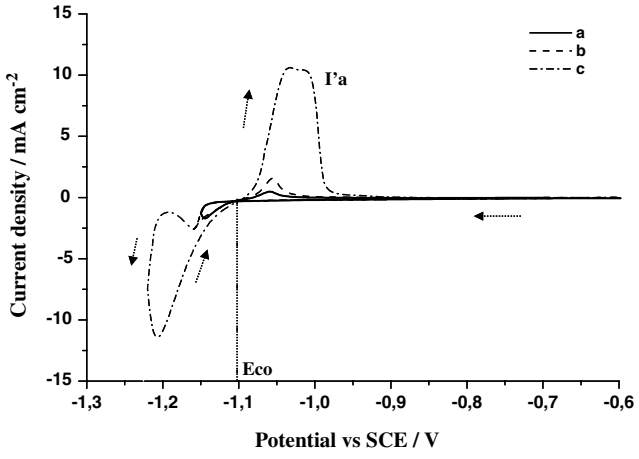

Fig. 4. Typical voltammograms for zinc nucleation on Pt, showing the crossover potential (Eco), obtained in solution S_0 containing 0.2 g l^{-1} BDA at different switching potentials (E_λ). (a) $E_\lambda = -1.13$, (b) $E_\lambda = -1.14$, (c) $E_\lambda = -1.22$ vs SCE/V.

Table 1. Values of the cathodic peak potential (E_P), crossover potential (Eco), and overpotential (η), associated with the reduction of zinc on Pt in solution S_0 with different concentrations of BDA

[BA]/g l^{-1}	*E*co vs SCE/V	$E_{PI'c}$ vs SCE/V	$\eta_{PI'c}$ ($E_{PI'c}$ − *E*co)/V	$E_{PII'c}$ vs SCE/V	$\eta_{PII'c}$ ($E_{PII'c}$ − Eco)/V
0.2	−1.101	−1.150	−0.049	−1.230	−0.129
0.3	−1.100	−1.150	−0.050	−1.290	−0.190

Without BA: $E_{PI'c}$ = −1.15 vs SCE/V; Eco = −1.094 vs SCE/V; η_{WBA} = −0.056/V.

phases deposited during the reduction processes I'c and II'c. In addition, as shown in Figure 4, Eco is independent of E_λ. The mean value of Eco was −1.10 vs SCE/V (see Table 1), which is close to the conditional potential of the $ZnCl_4^{2-}/Zn(0)$ system ($E'_{ZnCl_4^{2-}/Zn(0)} = -1.094$ vs SCE/V). These results indicate that the reduction processes giving rise to peaks I'c and II'c involve the soluble species $ZnCl_4^{2-}$, and from this, it can be concluded that BDA does not form complexes with Zn^{2+}.

Table 1 shows the values of the overpotential ($\eta \equiv E_{PI'c,PII'c}$−Eco, where $E_{PI'c,\ PII'c}$ corresponds to the potential of peak I'c or II'c) obtained for the reduction processes at different BDA concentrations. The overpotential associated with peak I'c ($\eta_{PI'c}$) is independent of the concentration of BDA. However, the absolute value of the overpotential for peak II'c ($\eta_{PII'c}$) increases with increasing BDA concentration. These findings suggest that BDA acts at the interface, blocking the discharge of the metal ions by creating a barrier in the vicinity of the electrode surface. For this reason, a higher activation energy is required for the bulk deposition of zinc. Thus, when BDA is present in the solution, the deposition of zinc onto Pt occurs via two reduction processes with different energies (I'c and II'c) that involve the same species, $ZnCl_4^{2}$ (Equation 1).

Table 2 shows the charges associated with the reduction processes in the absence and presence of BDA. The charge associated with each reduction process was obtained by integrating, over the appropriate potential interval, the curve of current density vs potential recorded during the potential scan in the cathodic direction. In the presence of BDA, the charge associated with peak I'c ($Q_{PI'c}$=2.52 μC cm^{-2}) is independent of the BDA concentration. This observation is consistent with BDA having reached its maximum degree of adsorption at both of the BDA concentrations used, leaving a constant quantity of vacant active sites for the growth of zinc crystals in this potential zone. In addition, the values of $Q_{PI'c}$ obtained in the presence of BDA are much lower than that obtained in the absence of the additive at the same potential (Q_{PIc}=81.7 μC cm^{-2}). These results indicate that the presence of BDA in solution causes a 96.9% drop in the reduction of zinc via the process giving rise to peak Ic. In addition, increasing the concentration of BDA in the solution causes a reduction in the charge associated with peak II'c. This effect is principally due to the displacement of peak II'c toward more cathodic potentials with increasing BDA concentration (see Figure 3).

3.2. *Chronoamperometric study*

We used chronoamperometry to identify the zinc nucleation mechanism at different potentials. This potentiostatic technique has proved to be a powerful tool for elucidating the mechanisms by which new phases form (electrocrystallization).

3.2.1. *Chronoamperometric study in the absence of BDA*

Figure 5a shows a family of transients recorded during the reduction of zinc in solution S_0 in the potential range −1.13 to −1.15 vs SCE/V, which corresponds to the potential of peak Ic in Figure 1. Hydrogen evolution does not interfere with the electrodeposition process under these conditions. The behavior of these transients is typical of a nucleation process with three-dimensional growth of nuclei limited by the diffusion of the electroactive species ($3D_{-dc}$) [28]. Each of the transients in Figure 5a exhibits an increase in current density up to a maximum followed by a decay that converges to the limiting current, which corresponds to linear diffusion of the electroactive ions to a planar electrode.

This behavior can be described by the theoretical model proposed by Tarallo et al. [29–31] for diffusion-controlled crystal nucleation and growth in three dimensions ($3D_{-dc}$) [32]:

$$i_{3D_{-dc}} = zFc\left(\frac{D}{\pi}\right)^{1/2}\left(\frac{\Phi}{\Theta t^{1/2}}\right)[1-\exp(-\pi k N_o D t \Theta)] \tag{3}$$

Table 2. Charge values associated with the reduction processes, $Q_{PI'c}$, $Q_{PII'c}$, total cathodic charge (*Q*c) and total anodic charge (*Q*a), obtained from the voltammograms recorded at different concentrations of BDA (Figure 3)

[BA]/gl^{-1}	$Q_{I'c}/\mu$ C cm^{-2}	$Q_{II'c}/\mu$ C cm^{-2}	Q_c ($Q_{I'c}$ + $Q_{II'c}$)/μ C cm^{-2}	Q_a/μ C cm^{-2}
0.2	2.52	71.08	73.08	73.04
0.3	2.52	58.01	60.61	59.55

Without BA: Q_c = 81.70/μ C cm^{-2} Q_a = 80.5/μ C cm^{-2}.

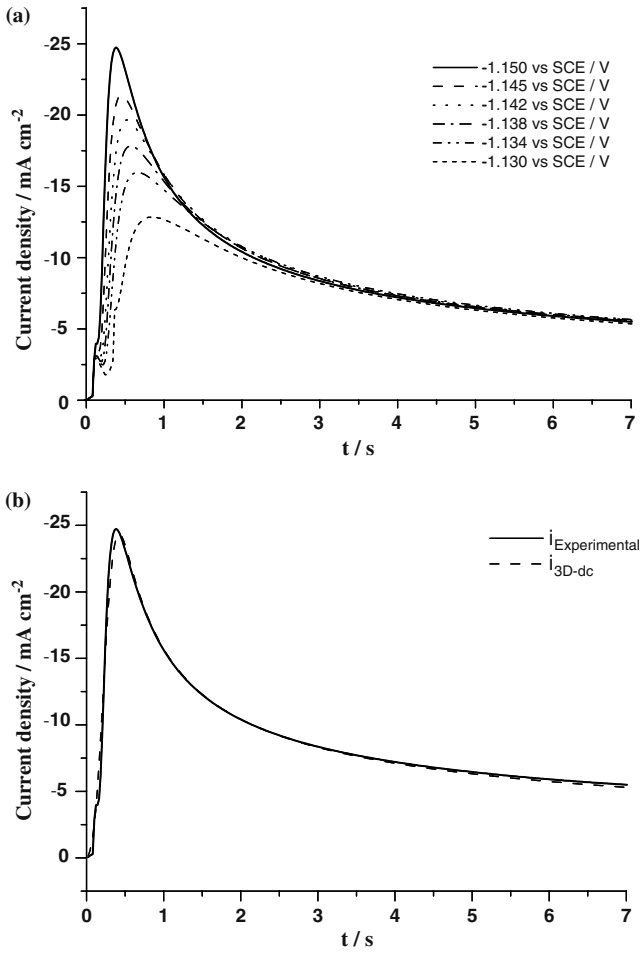

Fig. 5. (a) Typical family of potentiostatic transients obtained at different potentials during the reduction of zinc on Pt in solution S_0. (b) Comparison of an experimental transient recorded at $E = -1.150$ vs SCE/V with a typical transient obtained using Equation 3.

where

$$k = \left(\frac{8\pi cM}{\rho}\right)^{\frac{1}{2}} \tag{4}$$

$$\Theta = 1 - [1 - \exp(-At)]/At \tag{5}$$

$$\Phi \equiv \Phi[(At)^{\frac{1}{2}}]$$

related to Dawson's integral, is given by:

$$\Phi = 1 - \frac{\exp(-At)}{(At)^{1/2}} \int_0^{(At)^{1/2}} \exp \lambda^2 \mathrm{d}\lambda \tag{6}$$

Here, A is the nucleation rate constant, N_0 is the number density of active sites, D is the diffusion coefficient (for Zn^{2+} in solution S_0, $D = 3.06 \times 10^{-6}$ cm^2 s^{-1} [8]), c (mol cm^{-3}) is the concentration of metal ions in the solution, and M (g mol^{-1}) and ρ (g cm^{-3}) are the molecular weight and density of the metal respectively.

The fitting of Equation 3 requires the values of Φ and thus the values of Dawson's integral, which can be approximated by the rational function [30]:

$$F(x) \equiv e^{-x^2} \int^x e^{\lambda^2} \mathrm{d}\lambda \cong \frac{0.051314213 + 0.47910725x}{1 - 1.206812x + 1.185724x^2} \tag{7}$$

For the product $(\Phi/\Theta t^{1/2})$, Arbid et al. [33] have proposed the following equation:

$$\frac{\Phi}{\Theta t^{1/2}} = \frac{0.520893At^{1/2} - 1.206814A^{3/2}t + 1.185724A^2t^{3/2} - 0.051314A^{1/2}}{[At - 1 + \exp(-At)](1 - 1.206814A^{1/2}t^{1/2} + 1.185724At)} \tag{8}$$

Figure 5b shows a comparison between the experimental results for the transient obtained at $E = -1.15$ vs SCE/V and the nonlinear fit of Equation 3. It is clear from this figure that the nucleation of zinc in the absence of BDA conforms to the $3D_{-dc}$ model. Similar behavior was observed in all of the transients shown in Figure 5a. Table 3 shows the values of the kinetic parameters obtained from the fit of Equation 3. The nucleation rate (A) and the numerical density of active sites (N_0) both increases with increasing applied cathodic potential, behavior characteristic of diffusion-controlled 3D nucleation processes.

Figure 6 shows the AFM image of Zn deposited, corresponding to the transient shown in Figure 5b ($E = -1.15$ vs SCE/V, $t = 7$ s). This image shows that the Pt surface is completely covered with differently sized hexagonal crystals, indicative of progressive 3D nucleation. The rms surface roughness determined from the AFM scan was 44.47 nm. It is important to mention that the mechanism of Zn nucleation and growth is strongly affected by diverse factors, including zinc ion concentration, overpotential, and pH. As a result, any change in the deposition conditions can significantly alter the kinetics and morphology of nucleation. For example, Raeissi et al. [6] reported that, when the zinc concentration in solution was 2 M, the deposition of zinc occurred via diffusion-controlled instantaneous 3D nucleation and growth, which is different than the mechanism observed in the present work.

Table 3. Potential dependence of the kinetic parameters describing zinc nucleation on Pt

Potential vs SCE/V	A/s^{-1}	N_0 ($\times 10^{-7}$)/cm^{-2}
−1.130	0.43	0.025
−1.135	0.47	0.039
−1.140	1.32	0.087
−1.145	1.54	0.152
−1.150	2.39	0.219

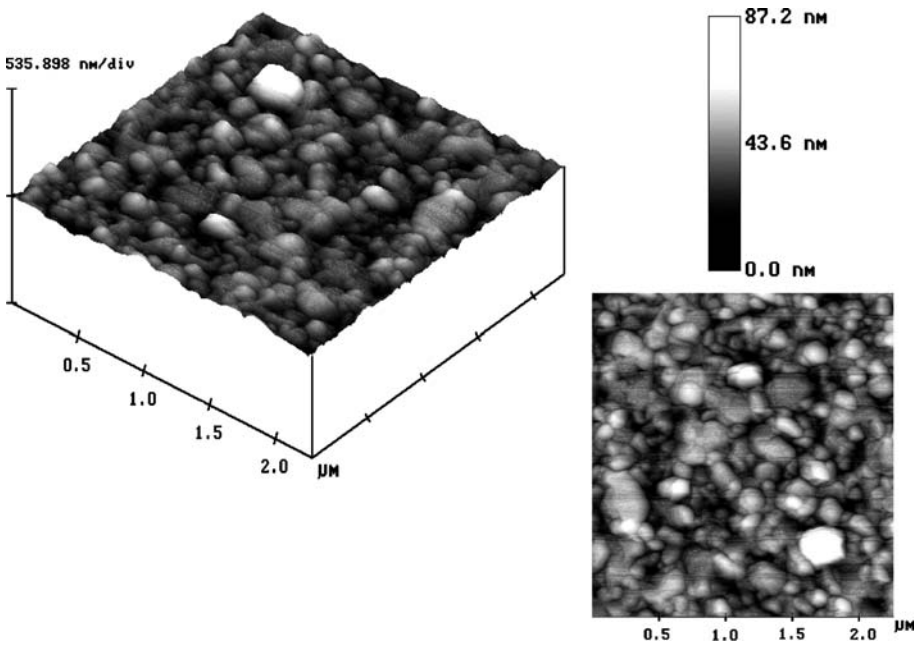

Fig. 6. An AFM image of zinc deposition onto Pt at −1.15 vs SCE/V, $t = 7$ s, in solution S_0; top view representations are also shown.

3.2.2. *Chronoamperometric study in the presence of BDA*
In the presence of 0.2 g l^{-1} BDA, different forms of the transients were obtained in the various potential intervals studied, indicating that the mechanism of zinc electrocrystallization in the presence of BDA depends on the applied potential. Figure 7a shows the potentiostatic transients obtained in the potential range −1.13 to −1.15 vs SCE/V (corresponding to the interval in which peak I'c appears in the voltammogram recorded in the presence of BDA; curve a, Figure 3). These transients exhibit a maximum (P1) in the current density, a feature characteristic of nucleation processes. Furthermore, analysis of the falling portion of the transient in Figure 7a using the Cottrell equation indicated that it does not converge to the limiting current density corresponding to linear diffusion to a planar electrode, and therefore that the required diffusion control never appeared. Thus to identify the mechanism of zinc nucleation under these conditions, we used the theoretical curve model for crystal nucleation and growth in two dimensions controlled by lattice incorporation of adatoms ($2D_{-li}$) proposed by Bewick et al. [34], for two limiting cases: progressive nucleation ($2D_{p-li}$) and instantaneous nucleation ($2D_{i-li}$). These models are described by the following equations:

$$i_{2D_{p-li}(t)} = \frac{\pi z F M h A N_0 K_g^2 t^2}{\rho} \exp\left(\frac{-\pi A N_0 M^2 K_g^2 t^3}{3\rho^2}\right) \text{ (Progressive)} \quad (9)$$

$$i_{2D_{i-li}(t)} = \frac{2\pi z F M h N_0 K_g^2 t^2}{\rho} \exp\left(\frac{-\pi N_0 M^2 K_g^2 t^2}{\rho^2}\right) \text{ (Instantaneous)} \quad (10)$$

where N_0 is the number density of active sites, K_g is the lateral growth rate constant of nuclei, A is the

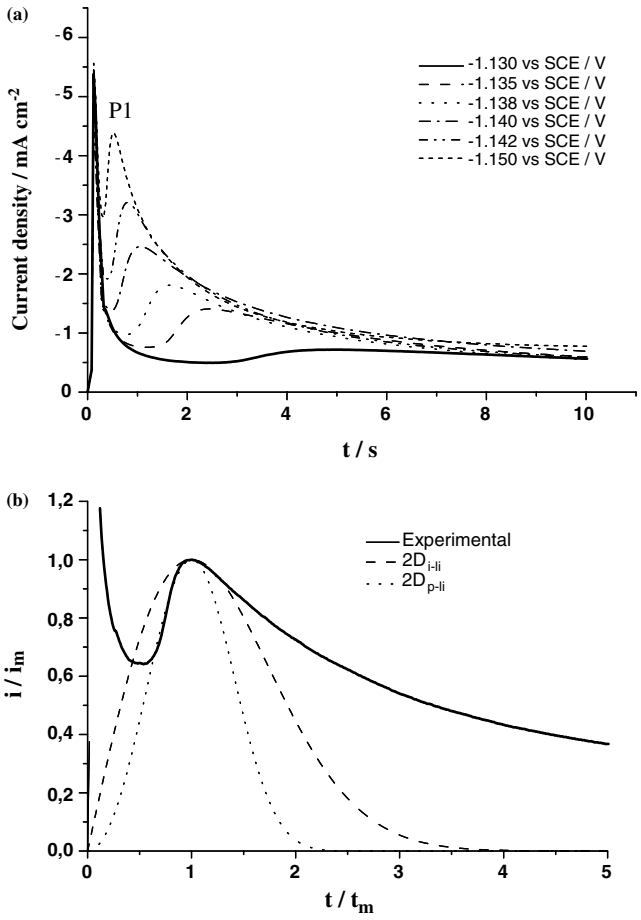

Fig. 7. (a) Typical family of potentiostatic transients obtained at different potentials during the reduction of zinc on Pt in solution S_0 + 0.2 g l^{-1} BDA. (b) Comparison of a dimensionless experimental plot recorded at $E = -1.138$ vs SCE/V with dimensionless plots for 2D nucleation controlled by the incorporation of adatoms obtained using Equations 11 and 12.

nucleation rate constant, M and ρ are the molar mass and the density of the metal respectively, zF is the molar charge transferred during the reduction process, and h is the monolayer thickness. Using the coordinates of the maxima of the transients (i_m, t_m), the above equations can be transformed into dimensionless expressions. Plots of these dimensionless expressions are commonly used to distinguish between progressive and instantaneous nucleation:

$$\frac{i}{i_m} = \left(\frac{t}{t_m}\right)^2 \exp\left[\frac{-2}{3}\left\{\frac{t^3 - t_m^3}{t_m^3}\right\}\right] \quad \text{(Progressive)} \quad (11)$$

$$\frac{i}{i_m} = \left(\frac{t}{t_m}\right) \exp\left[\frac{-1}{2}\left\{\frac{t^2 - t_m^2}{t_m^2}\right\}\right] \quad \text{(Instantaneous)} \quad (12)$$

Figure 7b shows the experimental data presented in dimensionless form along with the theoretical dimensionless curves obtained from Equations 11 and 12. The rising part of the experimental curve coincides very well with the theoretical curve for 2D progressive nucleation ($2D_{p-li}$). After the maximum, the experimental data more closely resemble the theoretical curve for 2D instantaneous nucleation ($2D_{i-li}$). Given that a transition from $2D_{p-li}$ to $2D_{i-li}$ is unlikely, these observations suggest that, in this zone, the total current in the chronoamperograms consists of contributions from both nucleation processes. It is important to observe that at long times the experimental data do not conform to either of the models, suggesting the presence of some other process. Similar results have been reported by Palomar-Pardavé et al. [35], who proposed, in accord with other authors [36–38], that 2D nucleation is usually followed by 3D nucleation. Following the method proposed by Palomar-Pardavé et al., we consider the total current of the transients as being comprised of contributions from three types of nucleation. For the systems considered here, we take the third nucleation process to be 3D progressive nucleation controlled by lattice incorporation of adatoms ($3D_{p-li}$) described by the following Equation [39]:

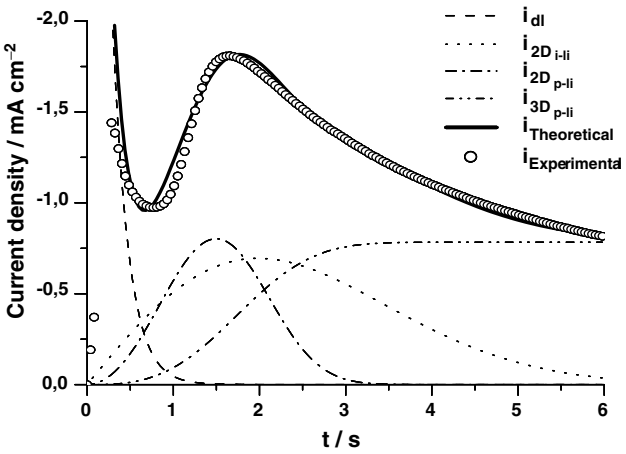

Fig. 8. Transient obtained experimentally at $E = -1.138$ vs SCE/V during the reduction of zinc on Pt in solution S_0 + 0.2 g l^{-1} BDA, along with the corresponding theoretical curve. The contributions to the transient from the double layer phenomenon (dl) and 2D and 3D nucleation controlled by the incorporation of adatoms, are shown separately.

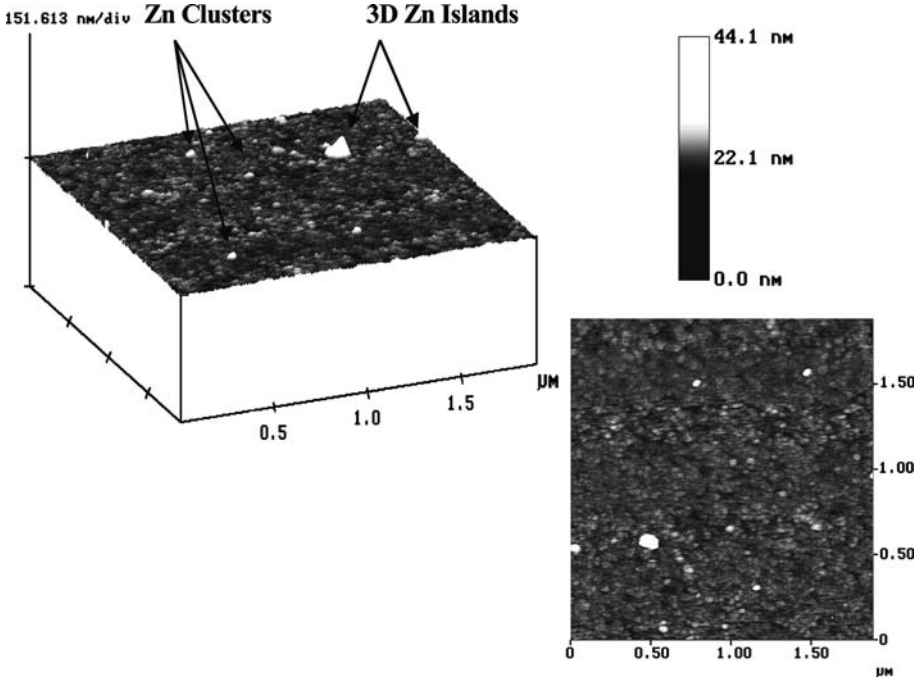

Fig. 9. An AFM image of zinc deposited onto Pt at −1.138 vs SCE/V, $t = 7$ s, in solution S_0 + 0.2 g l^{-1} BDA; top view representations are also shown.

$$i_{3D_{p-li}} = zFK'_g\left[1 - \exp\left(-\frac{\pi M^2 K_g^2 A N_0 t^3}{3\rho^2}\right)\right] \quad (13)$$

where K'_g is the vertical growth rate constant.

Based on the above arguments, we propose the following deconvolution of the total current density of the transients:

$$i_{theoretical} = i_{dl} + i_{2D_{p-li}} + i_{2D_{i-li}} + i_{3D_{p-li}} \quad (14)$$

where $i_{dl} = k_1 \exp(-k_2 t)$ is the current due to the effect of the double layer charge [37].

Figure 8 shows a comparison of the experimental transient obtained during the nucleation of zinc at −1.138 vs SCE/V and the nonlinear fit of Equation 14. The fit is good, and similar behavior was observed for all of the transients in Figure 7a. It is seen that current density maxima can be associated to an progressive 2D nucleation process limited by lattice incorporation of zinc adatoms, with a strong contribution from instantaneous 2D nucleation. Furthermore, from Figure 8 we see that the two $2D_{-li}$ processes are faster than the $3D_{-li}$ process, indicating that the final part of the transient is mainly due to the contribution of 3D nucleation (limited by lattice incorporation of adatoms) to the total current density. This characteristic could explain why the Cottrell equation does not describe the falling portion of this kind of transient.

2D nucleation observed during zinc deposition is only justified if the underpotential deposition (UPD) of Zn(II) ions on Pt occurs, that is, if the binding energy between Zn and Pt (Zn–Pt) is greater than that between the deposited atoms (Zn–Zn) [40]. This characteristic has been demonstrated by Aramata et al. [41–44], who studied the UPD of Zn^{2+} ions onto Pt using diverse techniques.

Figure 9 shows the AFM image of Zn deposited, corresponding to the transient shown in Figure 8 ($E = -1.138$ vs SCE/V, $t = 6$ s). The AFM image shows evidence of two types of crystal growth, one corresponding to the formation of small, similarly-sized hexagonal crystals (diameter of ~85 nm and height of ~11 nm) growing parallel to the surface, and the second corresponding to the growth of islands (2) in three dimensions made up of hexagonal crystals (diameter of ~156 nm and height of ~60 nm). The observed behavior might indicate that a competition exists between the rates of lateral and vertical growth of the crystals. To short times, the rate of lateral growth prevails on the rate of vertical growth, whereas to long times the opposite happens. It is important to mention that the crystal growth observed in this potential interval corresponds to the formation of crystals on the active sites that are not blocked by BDA (peak I'c, curve a, Figure 3). This behavior confirms the additive-induced inhibition of zinc reduction in this potential interval observed in the voltammetric study.

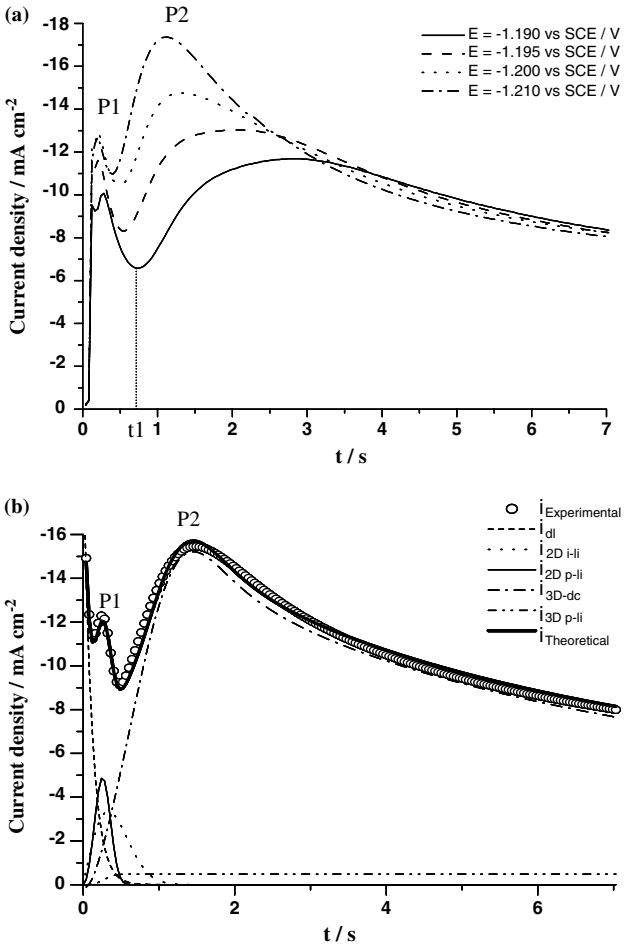

Fig. 10. (a) Typical family of potentiostatic transients obtained at different potentials during the reduction of zinc in the potential interval −1.19 to −1.21 vs SCE/V in solution S_0 + 0.2 g l^{-1} BDA. (b) Transient obtained experimentally at $E = -1.21$ vs SCE/V and the corresponding theoretical curve. The contributions of the different nucleation processes are shown separately.

When the applied potential was sufficiently cathodic to cause the desorption of the BDA from the Pt surface, an important change was observed in the transients. Figure 10a shows the family of transients obtained when the potential pulses were performed in the potential range −1.190 to −1.21 vs SCE/V (corresponding to the potential interval in which peak II'c appears in the voltammogram obtained in the presence of BDA; curve a, Figure 3). In the time interval $0 < t < t1$, a predeposit is formed via 2D nucleation (peak P1) that is the same as that observed in the previous potential interval (−1.13 to −1.15 vs SCE/V). After an induction time during which BDA is desorbed from the Pt surface, a new nucleation and growth process in three dimensions is observed. The current density reaches a maximum (peak 2), and then decreases slowly compared to the rising part of the transient. This new crystal nucleation and growth process occurs at the active sites vacated as a result of the desorption of BDA. We analyzed these experimental data using the same methodology as was employed in the analysis of peak P1 except that, in view of the form of the transients, in this case we included an

additional nucleation process, 3D diffusion-controlled nucleation ($3D_{-dc}$). With the inclusion of this additional process, the total current density of the transients in this potential range is given by the following expression:

$$i_{\text{theoretical}} = i_{\text{dl}} + i_{2D_{p-li}} + i_{2D_{i-li}} + i_{3D_{p-li}} + i_{3D_{-dc}} \qquad (15)$$

Figure 10b shows the experimental results along with the nonlinear fit of Equation 15. Interestingly, the fits indicate that the processes involved occur consecutively but with strong overlapping. At short times, the first nucleation process (P1) occurs via two 2D nucleation processes limited by lattice incorporation of adatoms ($2D_{-li}$), with 2D progressive nucleation dominating.

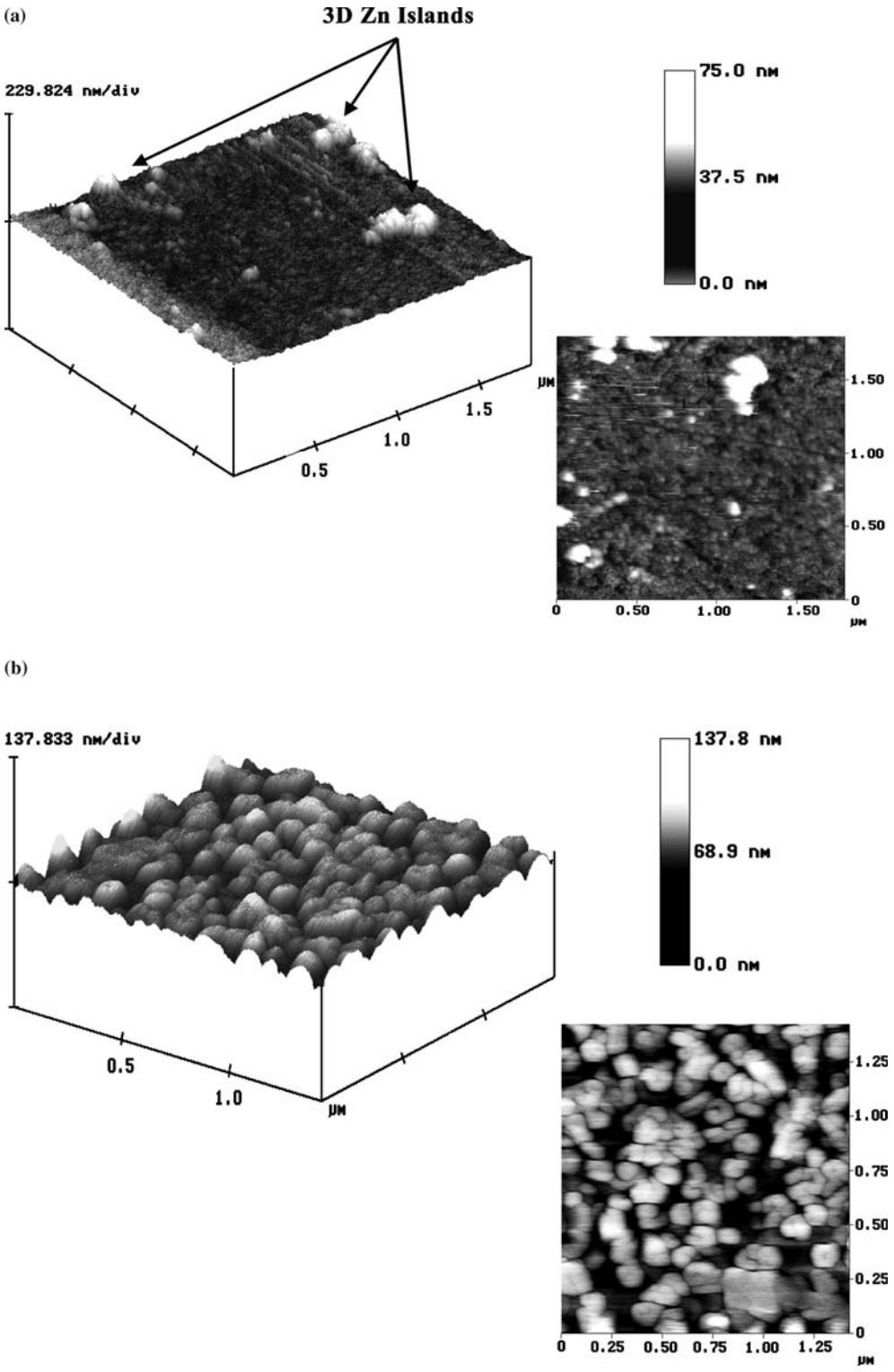

Fig. 11. AFM images of zinc deposition onto Pt at −1.21 vs SCE/V, in solution S_0 + 0.2 g l^{-1} BDA; top view representations are also shown. (a) $t = 0.85$ s, (b) $t = 7.0$ s.

Table 4. Kinetic parameters obtained by the nonlinear fitting of Equation 15 to the potentiostatic transients shown in Figure 10b

Potential vs SCE/V	dl		$2D_{i-li}$		$2D_{p-li}$		$3D_{i-li}$		$3D_{-dc}$	
	k_{1dl} ($\times 10^2$)/ A cm^{-2}	k_{2dl} ($\times 10^8$)/ s^{-1}	h ($\times 10^8$)/cm	$N_0K_g^2$ ($\times 10^2$)/ mol^2 cm^{-6} s^{-2}	h ($\times 10^8$)/cm	$AN_0K_g^2$ ($\times 10^{-7}$)/ mol^2 cm^{-6} s^{-2}	K'_g ($\times 10^8$)/ mol^2 cm^{-6} s^{-2}	$AN_0K_g^2$ ($\times 10^{-7}$)/ mol^{2}cm^{-6}s^{-2}	A/s^{-1}	N_0 ($\times 10^{-7}$)/cm^{-2}
−1.190	2.06	8.3	25.0	0.28	9.40	0.18	1.69	0.96	0.17	0.095
−1.195	1.99	8.4	18.8	0.55	7.50	0.37	1.95	15.14	0.19	0.215
−1.200	1.98	8.7	8.8	1.70	5.81	0.45	2.50	35.41	0.24	0.285
−1.205	1.96	8.5	5.5	2.42	5.51	0.50	3.70	79.37	0.27	0.365

After this initial rise, a new nucleation and growth process becomes dominant. This new process is made up of two main contributions: a major contribution from $3D_{-dc}$ nucleation and a lesser contribution from $3D_{p-li}$ nucleation. Similar results were observed for the other BDA concentration studied. The values of the kinetic parameters obtained are shown in Table 4; these values are comparable with those reported for other systems [35, 37]. The nucleation rates of all of the processes increase as the applied potential is made more cathodic.

Figure 11 shows the AFM images of Zn deposited, obtained in different regions of the transient shown in Figure 10a. The AFM image obtained at −1.21 vs SCE/V and $t = 0.80$ s (Figure 11a), which corresponds to the rising portion of peak 2 in Figure 10b, shows a surface structure comprised of 3D islands of Zn. In addition, the AFM image reveals a change in the substrate surface, likely due to the desorption of BDA from the Pt surface. The AFM image recorded at $t = 7$ s (Figure 11b), which corresponds to the final part of the transient, shows regularly-sized, nodule-like clusters covering the majority of the Pt surface. In this way, the bulk deposition of zinc occurs over the Pt surface after the BDA has been desorbed from the surface. The rms surface roughness was 8.99 nm.

4. Conclusions

We have shown that the presence of BDA in a solution in which zinc is being reduced on Pt modifies the zinc reduction process. Comparison of the values of Eco and the conditional potential ($E'ZnCl_4^{2-}/Zn(0)$) calculated for the couple $ZnCl_4^{2-}/Zn(0)$ revealed that BDA does not form complexes with Zn under the working conditions used in the present experiments, indicating that this additive principally acts at the Pt surface. The cyclic voltammetry results revealed that BDA partially inhibits the reduction of zinc, leading to two reduction processes (peaks I'c and II'c) with different energies that involve the same species, $ZnCl_4^{2-}$.

To elucidate the kinetics of zinc electrocrystallization in the absence and presence of BDA, we carried out a chronoamperometric study in which we analyzed potentiostatic transients at different potential intervals. The results indicated that in the absence of BDA, zinc nucleation occurs *via* diffusion-controlled nucleation in three dimensions ($3D_{-dc}$). In the presence of BDA, the transients exhibited a complex form that depended on the applied potential. In the potential interval 1.13 to −1.15 vs SCE/V, a process (P1) is observed that can be explained as a combination of three nucleation and growth processes: 2D progressive, 2D instantaneous, and 3D progressive nucleation, each limited by the incorporation of adatoms. Process P1 occurs at the few active sites on the Pt surface that are not blocked by adsorbed BDA.

When the transients were obtained at more cathodic potentials, in the potential interval corresponding to

peak II'c observed during the voltammetry study, the desorption of BDA from the Pt surface occurred and two crystal nucleation and growth processes (P1 and P2) were observed. In this system, the deposition of one fraction monolayer (P1) is followed by three dimensional growth of a bulk deposit (P2) of Zn.

Characterization of the surface morphologies of the zinc deposits by AFM imaging confirmed our conclusions drawn from the electrochemical studies. The AFM images revealed that the morphology of the deposited zinc varied depending on the applied electrode potential. Comparison of the rms surface roughness values of the zinc deposits obtained in the absence and presence of BDA showed that addition of BDA reduced the roughness from 44.458 to 8.99 nm, demonstrating that the deposits formed in the presence of BDA are softer.

Acknowledgement

The authors are grateful for financial assistance provided by CONACyT (Consejo Nacional de Ciencia y Tecnología), México, Proyecto 39732. P. Díaz-Arista, also acknowledge CONACyT for scholarships.

References

1. G. Barceló, M. Sarret, C. Müller and J. Pregonas, *Electrochim. Acta*. **43** (1988) 13.
2. S. Rajendran, S. Bharanti and C. Krishna, *Plat. Surf. Finish*. **84** (October 1997) 53.
3. A.Y. Hosny, M.E. El-Rofei, T.A. Ramadan and B.A. El-Gafari, *Metal Finish*. **93** (November 1995) 55.
4. K.L. Lin, C.F. Yang and J.T. Lee, *Corrosion* **47** (1991) 9.
5. B. Bozzini, V. Accardi, P.L. Cavalloti and F. Pavan, *Metal Finish*. **97** (May 1999) 33.
6. K. Raeissi, A. Saatchi and M.A. Golozar, *J. Appl. Electrochem*. **33** (2003) 635.
7. J. Yu, L. Wang, L. Su, X. Ai and H. Yang, *J. Electrochem. Soc*. **150** (2003) C19.
8. G. Trejo, R. Ortega Borges, Y. Meas, V.E. Chainet, B. Nguyen and P. Ozil, *J. Electrochem. Soc*. **145** (1998) 4090.
9. D.D.N. Singh, M Dey and V. Singh, *Corrosion* **58** (2002) 971.
10. M. Sanchez Cruz, F. Alonso and J.M. Palacios, *J. Appl. Electrochem*. **23** (1993) 364.
11. J. Yu, H. Yang, X. Ai and Y. Chen, *Russian J. Electrochem*. **38** (2002) 363.
12. D.S. Baik and D.J. Fray, *J. Appl. Electrochem*. **31** (2001) 1141.
13. D. Mockute and G. Bernotiene, *Chemija* **2** (1996) 90.
14. G. Bernotiene and D. Mockute, *Russian J. Electrochem*. **30** (1994) 146.
15. G. Trejo, R. Ortega, Y. Meas, E. Chainet and P. Ozil, *J. Appl. Electrochem*. **33** (2003) 373.
16. L. Joo-Yul, K. Jae-Woo, L. Min-Kyu, S. Hyun.Joon, K. Hyun-Tae and P. Su-Moon, *J. Electrochem. Soc*. **151** (2004) C25.
17. K. Jae-Woo, L. Joo-Yul and P. Su-Moon, *Langmuir* **20** (2004) 459.
18. V. Danciu, V. Cosoveanu, E. Grunwald and G. Oprea, *Galvanotechnik* **94** (2003) 566.
19. Juhos, S. Mathe, E. Gruenwald, C. Varhelyi and G. Sfintu, *Galvnotechnik* **83** (1992) 2282.
20. D. Mockute and G. Bernotiene, *J. Appl. Electrochem*. **27** (1997) 691.
21. S. Fletcher, *Electrochim. Acta* **28** (1983) 917.
22. S. Fletcher, C.S. Halliday, D. Gates, M. Westcott, T. Lwin and G. Nelson, *J. Electroanal. Chem*. **159** (1983) 267.
23. G. Gunawardena, G. Hills and I. Montenegro, *J. Electroanal. Chem*. **138** (1982) 241.
24. C. Nila and I. González, *J. Electroanal. Chem*. **401** (1996) 171.
25. M. Miranda-Hernández and I. González, *Electrochim. Acta*. **42** (1997) 2295.
26. L. Oniciu and L. Muresan, *J. Appl. Electrochem*. **21** (1991) 565.
27. T.C. Franklin, *Surf. and Coat. Tech*. **30** (1987) 415.
28. B.R. Scharifker and G. Hills, *Electrochim. Acta* **28** (1983) 879.
29. Heerman and A. Tarallo, *J. Electroanal. Chem*. **470** (1999) 70.
30. L. Heerman and A. Tarallo, *J. Electroanal. Chem*. **451** (1998) 101.
31. A. Milchev and L. Heerman, *Electrochim. Acta* **48** (2003) 2903.
32. L. Heerman and A. Tarallo, *Electrochem. Comm*. **2** (2000) 85.
33. M. Arbid, B. Zhang, V. Lazarov, D. Stoychev, A. Milchev and C. Buess-Herman, *J. Electroanal. Chem*. **510** (2001) 67.
34. A. Bewick, M. Fleischmann and H.R. Thirsk, *Faraday Soc*. **58** (1962) 2200.
35. M. Palomar-Pardavé, I. González, A.B. Soto and E.M. Arce, *J. Electroanal. Chem*. **443** (1998) 125.
36. M.Y. Abyaneh and M. Fleishmann, *J. Electroanal. Chem*. **119** (1981) 187.
37. M. Palomar-Pardavé, M. Miranda-Hernández, I. González and N. Batina, *Surf. Sci*. **399** (1998) 80.
38. N. Batina, A. Martínez-Ruíz, M. Palomar-Pardavé, J. Valenzuela-Benavides and M.H. Farías, *J. Phys. Chem*. **107** (2003) 11660.
39. R.D. Armstrong, M. Fleischmann and H.R. Thirsk, *J. Electroanal. Chem*. **11** (1966) 208.
40. G. Staikov, W.J. Lorenz, and E. Bidevski, Low-dimensional metal phases and nanostructuring of solid surfaces, *in* J. Lipkowski and P.N. Ross, "Imaging of Surfaces and Interfaces" (Eds) (WILEY-VCH, New York, 1999), pp. 1–56.
41. S. Taguchi and A. Aramata, *J. Electroanal. Chem*. **396** (1995) 131.
42. G. Horángy and A. Aramata, *J. Electroanal. Chem*. **434** (1997) 201.
43. A. Aramata, Md.A. Quaiyyum, W.A. Balais, T. Atoguchi and M. Enyo, *J. Electroanal. Chem*. **338** (1992) 367.
44. S. Takahashi, A. Aramata, M. Nakamura, K. Hasebe, M. Taniguchi, S. Taguchi and A. Yamagishi, *Surf. Sci*. **512** (2002) 37.